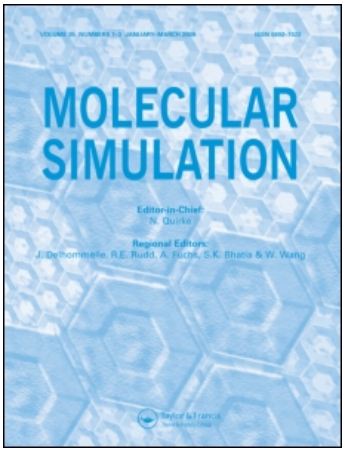


**Molecular Simulation**
Publication details, including instructions for authors and subscription information:
http://www.informaworld.com/smpp/title~content=t713644482

# Cats, maps and nanoflows: some recent developments in nonequilibrium nanofluidics

B. D. Todd[a]
[a] Centre for Molecular Simulation, Swinburne University of Technology, Hawthorn, Victoria, Australia

**To cite this Article** Todd, B. D.(2005) 'Cats, maps and nanoflows: some recent developments in nonequilibrium nanofluidics', Molecular Simulation, 31: 6, 411 — 428
**To link to this Article: DOI:** 10.1080/08927020412331332730
**URL:** http://dx.doi.org/10.1080/08927020412331332730

*Molecular Simulation*, Vol. 31, Nos. 6–7, 15 May – 30 May 2005, 411–428

Taylor & Francis
Taylor & Francis Group

# Cats, maps and nanoflows: some recent developments in nonequilibrium nanofluidics

B.D. TODD*

Centre for Molecular Simulation, Swinburne University of Technology, PO Box 218, Hawthorn, Victoria 3122, Australia

A review of some recent advances focusing on the problem of nano-scale fluids far from equilibrium modelled by nonequilibrium molecular dynamics (NEMD) is presented. It will be demonstrated how novel materials such as dendrimers can be successfully modelled using NEMD methods and how the distortion of their geometry by the imposed field has a significant influence on the transport properties of such fluids. Furthermore, it will be shown how a famous chaotic mapping scheme—the Arnold cat map—can be usefully employed for molecular dynamics (MD) simulations of an important industrial flow, namely elongational flow. This is the first connection ever made between the use of discrete dynamical chaotic maps and a practical application in MD simulations. It also highlights the problem that elongation is a highly unstable flow. Finally, a nonlocal constitutive model for the transport coefficients of nano-confined fluids (e.g., flows in nanoporous materials) is implemented. It is shown how such a model can be used to compute an effective shear viscosity for inhomogeneous fluids.

*Keywords*: Nonequilibrium molecular dynamics; Dendrimers; Shear flow; Elongational flow; Poiseuille flow; Chaos; Confined fluids; Nanofluidics



## 1. Introduction

The molecular simulation of fluids has, in recent years, become an exciting field of fundamental and applied research. On a fundamental level, problems in statistical mechanics and classical dynamics once thought intractable are now feasible with the aid of modern supercomputers. Advances made on this level include the study of systematic departures from conventional Navier–Stokes fluid dynamics on molecular length and timescales and the connection between statistical mechanics and the theory of dynamical systems (i.e., chaos). On the applied front, advances made in molecular simulation are allowing more refined predictions of the thermophysical, viscoelastic and transport properties of fluids for nanotechnological applications.

This paper serves as a review of three specific themes of simulation study recently performed by the author and colleagues: modelling of dendrimers under uniform shear at the molecular level, elongational flow and its relationship to dynamical systems and chaos, and the important nanotechnological problem of predicting meaningful transport properties for highly inhomogeneous fluids confined to nanometer dimensions. All three problems are inherently nonequilibrium in nature in that they involve fluids under various flow geometries, and all draw upon different simulation algorithms incorporating the techniques of nonequilibrium molecular dynamics (NEMD).

The review is structured as follows: in "Dendrimers under homogeneous shear" section, a brief background to dendrimers and how they are modelled is presented. Results for their structural and viscoelastic properties as computed by homogeneous NEMD simulations are then given and compared to traditional linear polymers of equivalent molecular weight. In "The Arnold cat map and elongational flow" section, the problem of simulating elongational flow with conventional NEMD is addressed. This problem is solved by use of suitable periodic boundary conditions and a connection is made with the Arnold cat map and dynamical systems theory. Use of the cat map formalism greatly simplifies the derivation of the necessary simulation parameters and furthermore highlights the unstable nature of elongational flow. In "Inhomogeneous flow and nanofluidics" section NEMD methods are applied to simulate inhomogeneous flow, namely Poiseuille flow of a simple fluid confined in a narrow channel of several atomic diameters width.

*E-mail: btodd@swin.edu.au

*Molecular Simulation*
ISSN 0892-7022 print/ISSN 1029-0435 online © 2005 Taylor & Francis Group Ltd
http://www.tandf.co.uk/journals
DOI: 10.1080/08927020412331332730

It is shown how classical Navier–Stokes behaviour breaks down on this length scale, and how an effective shear viscosity can be computed from a nonlocal constitutive equation. Finally in "Conclusions" section some concluding remarks are made and future research directions indicated.

## 2. Dendrimers under homogeneous shear

Dendrimers are a specialized highly branched synthetic polymer. Their internal structure consists of a central core with relatively short linear chains branching outward. With each new generation the dendrimer grows with a tree-like fractal structure. This structure is characterized by the number of generations ($g$; i.e., the number of "layers" of the dendrimer), the functionality of the end groups ($f$; i.e., how many branches per growth node) and the number of monomers in each individual chain unit ($b$). A schematic two-dimensional diagram of dendrimers of generation 1 to 3, functionality of 3 and $b = 2$ is shown in figure 1. Increasing the generation number results in a three-dimensional structure with a high degree of spherical symmetry.

The unique molecular architecture of dendrimers is touted as being potentially useful in nanotechnology, such as new chemical sensors, microscopic drug delivery systems and novel nanoscale materials. A further potential application is to exploit their unique transport properties. Their rheological properties differ significantly from traditional linear polymers due to their high spherical symmetry. This leads to the possibility of using them as rheology modifiers, processing aids, or nanoscale lubricants. For a concise discussion on relevant experimental, theoretical and simulation studies that have been performed on dendrimer solutions and melts, see [1,2]. In contrast to most simulation studies of dendrimers in solution, our studies have focused on dense dendrimers in the melt.

### 2.1 Model and simulation method

We model both dendrimers and linear polymers as coarse-grained beads representing monomeric units, constrained to adjacent beads by means of the finitely extensible nonlinear elastic (FENE) harmonic potential [3,4]

$$\begin{aligned} \phi_{ij}^{\mathrm{FENE}} &= 0.5kR_0^2 \ln[1 - (r_{ij}/R_0)^2] \quad \text{for } r_{ij} \le R_0 \\ \phi_{ij}^{\mathrm{FENE}} &= \infty \qquad\qquad\qquad\qquad\quad \text{for } r_{ij} > R_0 \end{aligned} \tag{1}$$

where the parameters $R_0 = 1.5$ and $k = 30$ (reduced units) are set to be in conformity with comparable simulation studies in the literature. Here $r_{ij}$ is the distance between adjacent intramolecular beads $i$ and $j$.

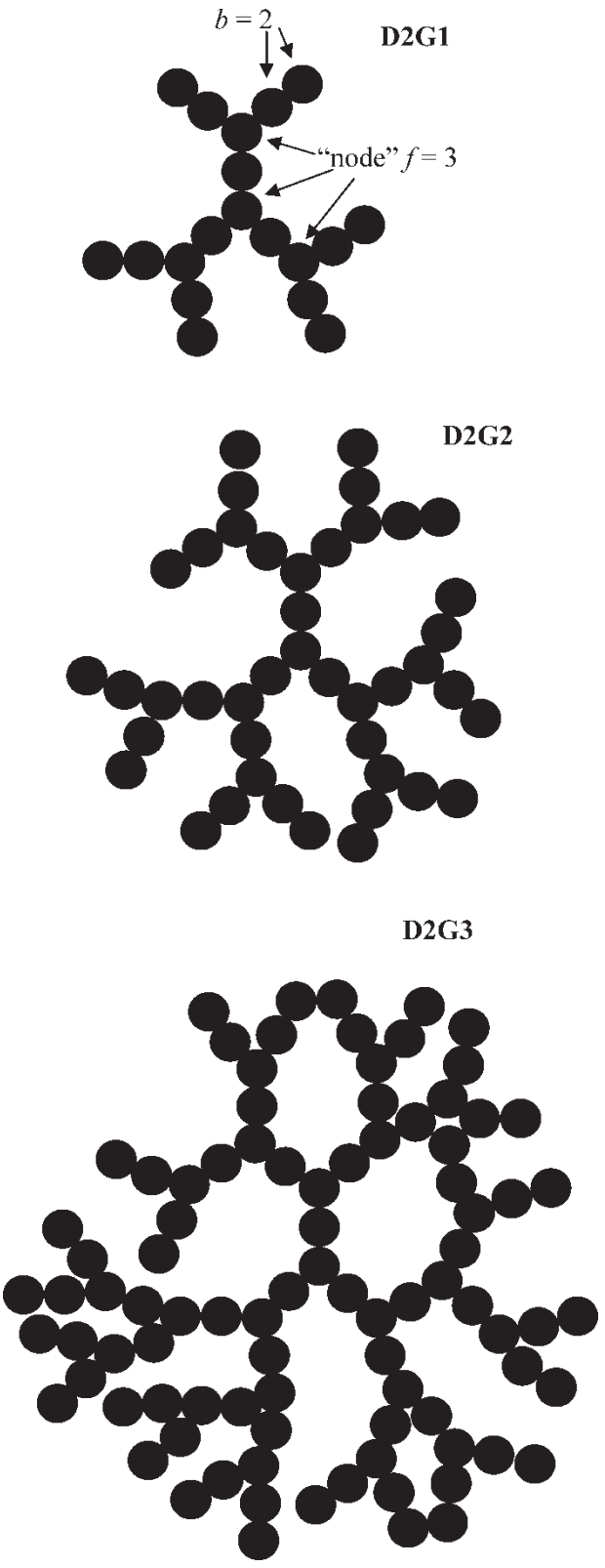


Figure 1. Two dimensional schematic representation of dendrimers of generation 1–3 with functionality $f = 3$ and spacers $b = 2$.

Our systems are modelled at a reduced density and temperature of 0.84 and 1.25, respectively. At this temperature the average reduced distance between the connected beads at equilibrium is approximately 0.97.

All beads are able to interact with beads on the same molecule or beads on other molecules via the shifted and truncated Lennard–Jones potential, commonly known as the Weeks–Chandler–Andersen (WCA) potential [5]

$$\begin{aligned} \phi_{ij}^{\mathrm{LJ}} &= 4\varepsilon\left[\left(\tfrac{\sigma}{r_{ij}}\right)^{12}-\left(\tfrac{\sigma}{r_{ij}}\right)^{6}\right]+\varepsilon \quad \text{for } r_{ij}/\sigma < 2^{1/6} \\ \phi_{ij}^{\mathrm{LJ}} &= 0 \qquad\qquad\qquad\qquad \text{for } r_{ij}/\sigma \geq 2^{1/6} \end{aligned} \tag{2}$$

$\varepsilon$ is the potential well depth and $\sigma$ is the effective diameter of the beads. $\varepsilon$ and $\sigma$ are assigned to unity and all derived quantities throughout the rest of this paper are expressed in reduced units relative to the Lennard–Jones parameters: $r_{ij}^{*} = r_{ij}/\sigma$, density $\rho^{*} = \rho\sigma^{3}$, temperature $T^{*} = k_{\mathrm{B}}T/\varepsilon$, pressure tensor $\mathbf{P}^{*} = \mathbf{P}\sigma^{3}/\varepsilon$, strain rate $\dot{\gamma}^{*} = (m\sigma^{2}/\varepsilon)^{1/2}\dot{\gamma}$, viscosity $\eta^{*} = (\sigma^{4}/m\varepsilon)^{1/2}\eta$. For simplicity of notation, hereafter the asterisk will be omitted.

Our model dendrimers of generations 1–4 were constructed with $f = 3$ and $b = 2$. Such a model results in 19, 43, 91 and 187 beads per single dendrimer (henceforth referred to as D2G1, D2G2, D2G3, and D2G4, respectively). The length of the linear polymers studied corresponded to the mass of the corresponding dendrimers, i.e. 19-mers, 43-mers, 91-mers, and 187-mers. System sizes ranged from 256 molecules for D2G1 and 19-mers to 125 molecules for larger molecules.

Planar shear flow (otherwise known as planar Couette flow) was generated by applying the molecular version of the homogenous isothermal shear algorithm (SLLOD) [6] in conjunction with standard Lees–Edwards periodic boundary conditions [7]. The equations of motion for bead $\alpha$ in molecule $i$ are given by

$$\begin{aligned} \dot{\mathbf{r}}_{i\alpha} &= \frac{\mathbf{p}_{i\alpha}}{m_{i\alpha}} + \mathbf{i}\dot{\gamma}y_i \\ \dot{\mathbf{p}}_{i\alpha} &= \mathbf{F}_{i\alpha} - \mathbf{i}\tfrac{m_{i\alpha}}{M_i}\dot{\gamma}p_{yi} - \zeta^{M}\tfrac{m_{i\alpha}}{M_i}\mathbf{p}_i \end{aligned} \tag{3}$$

where $\mathbf{r}_{i\alpha}$ and $\mathbf{p}_{i\alpha}$ represent the position and thermal (peculiar) momentum of bead $\alpha$ on molecule $i$, $\mathbf{p}_i$ is the momentum of the molecular centre of mass of molecule $i$ and $M_i$ is the mass of molecule $i$. The strain rate is defined by $\dot{\gamma} = \partial u_x/\partial y$, where $\mathbf{u} = \mathbf{i}u_x$ is the fluid streaming velocity in the $x$-direction. The streaming velocity of the molecule is determined by the position of its centre of mass and has the form $\mathbf{i}\dot{\gamma}y_i$, where $y_i$ is the position of the molecular centre of mass. The simulations were performed at constant temperature using a molecular version of the Gaussian thermostat with a constraint multiplier $\zeta^{M}$ given by

$$\zeta^{M} = \frac{\sum_{i=1}^{N}(\mathbf{F}_i\cdot\mathbf{p}_i - \dot{\gamma}p_{xi}p_{yi})/M_i}{\sum_{i=1}^{N}\mathbf{p}_i^{2}/M_i} \tag{4}$$

where $N$ is the number of molecules in the system. The thermostat constrains the molecular kinetic temperature of the systems defined as

$$\sum_{i=1}^{N_m}\frac{\mathbf{p}_i\cdot\mathbf{p}_i}{2M_i} = \frac{3N-4}{2}k_{\mathrm{B}}T_{\mathrm{M}}. \tag{5}$$

All simulations were performed at a molecular temperature $T_{\mathrm{M}} = 1.25$. The algorithm and thermostatting mechanism have been discussed in detail by Edberg *et al.*, [8] and Travis *et al.* [9]. Further details of our simulations may be found in [1,2].

### 2.2 Results and discussion

In what follows, a summary of the most interesting results gleaned from our recent work is presented. A more thorough discussion of the structural and rheological properties of dense dendrimer melts may be found in [1,2]. What sets dendrimers apart from more conventionally architectured molecules is their compact, tree-like fractal structure. Under flow conditions the overall spherical shape of the molecule deforms to an ellipse, with the axes of stretching and compression aligning with respect to the flow velocity streamlines. One can analyse the deformation of dendrimers by computing the radius of gyration tensor and its associated eigenvalues. The average squared tensor of gyration is given as

$$\mathbf{R}_{\mathbf{g}}^{2} \equiv \left\langle \frac{\sum_{\alpha=0}^{n} m_\alpha(\mathbf{r}_\alpha - \mathbf{g})(\mathbf{r}_\alpha - \mathbf{g})}{\sum_{\alpha=0}^{n} m_\alpha} \right\rangle \tag{6}$$

where $\mathbf{g}$ is the position of the molecular centre of mass, $\langle\ldots\rangle$ denotes an ensemble average and the index $\alpha$ runs over all monomer units of a particular dendrimer. The value of the squared radius of gyration is defined as the trace of the tensor $\left(R_g^2 = Tr\left(\mathbf{R}_{\mathbf{g}}^{2}\right)\right)$, which can be compared with experimentally measured radial sizes of dendrimers.

One may compute the eigenvalues by two means: first, by computing the eigenvalues of $\mathbf{R}_{\mathbf{g}}^{2}$ and then averaging over the system ($L_{\mathrm{i}}$), and second, by computing the eigenvalues of $\langle\mathbf{R}_{\mathbf{g}}^{2}\rangle$ and then orthogonalising ($L_{\mathrm{i}}'$). The former method gives the average linear dimensions of the molecular "ellipsoid". Due to their directional specificity, these average eigenvalues will not be equal at equilibrium for lower generation dendrimers, but will converge to unity as the dendrimer generation increases (i.e., as the molecule becomes more spherical in shape). As the fluid flows, the shape of the average molecule distorts, and so changes in the average eigenvalues with strain rate are indicative of flow induced stretching and alignment. In the latter method, orthogonalisation of the average tensor of gyration provides no information about molecular distortion; breaking of the spherical symmetry of these eigenvalues is related to the alignment of dendrimers with the flow field and can be directly related to birefringence experiments. Both sets of eigenvalues are shown in figure 2 for a third generation dendrimer, along with the shear viscosity defined as the ratio of the molecular stress to the strain rate. Of interest is that the onset of non-Newtonian behaviour (shear thinning) occurs at approximately the same strain rates as changes in slope of the averaged eigenvalues of the tensor of gyration ($L_{\mathrm{i}}$). This suggests that deformation of

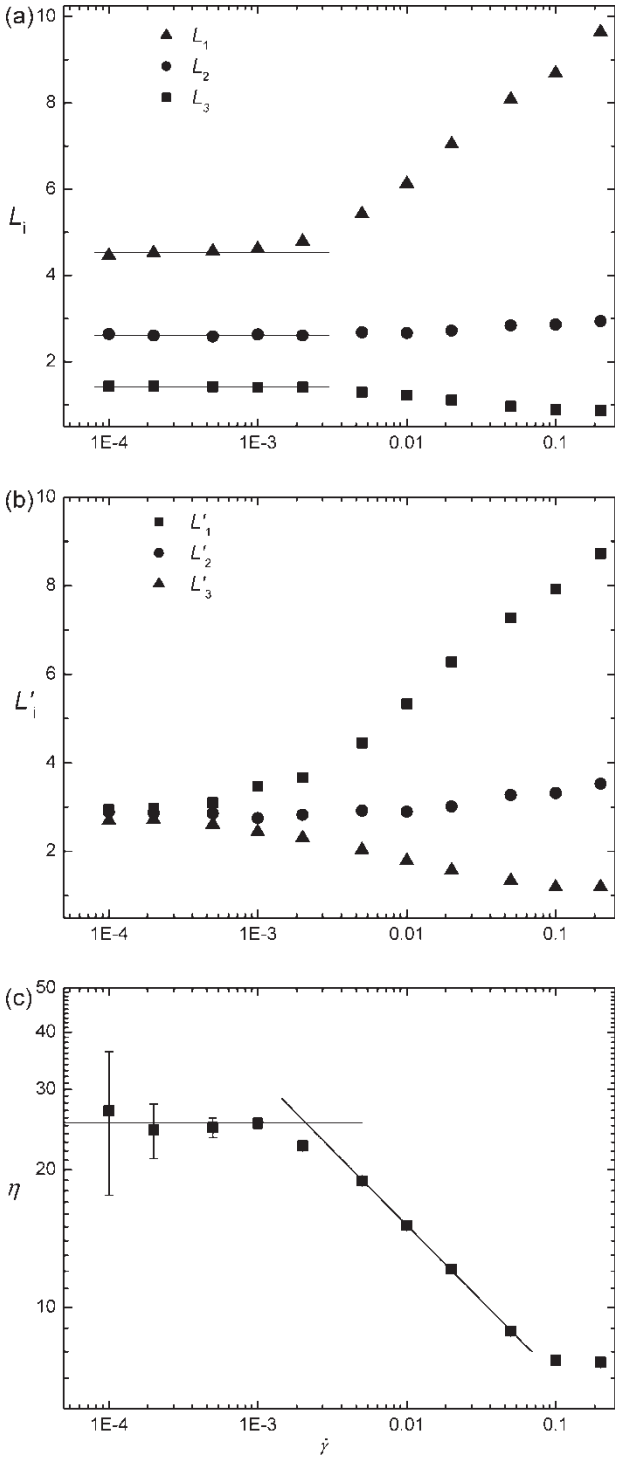


Figure 2. Eigenvalues of the squared radius of gyration tensor as a function of strain rate for a dendrimer of generation 3 by (a) computing the eigenvalues of $\mathbf{R}_g^2$ and then averaging over the system ($L_i$), and (b) by computing the eigenvalues of $\langle \mathbf{R}_g^2 \rangle$ and then orthogonalising ($L_i'$). Shear viscosity is shown in (c). Figure reproduced with permission from [1].

dendrimers is primarily responsible for the viscoelastic properties of the melt under flow, whereas molecular alignment, which occurs at all strain rates, seems to have a lesser influence.

One may analyse the degree of entanglement and back folding of intramolecular dendrimer branches by

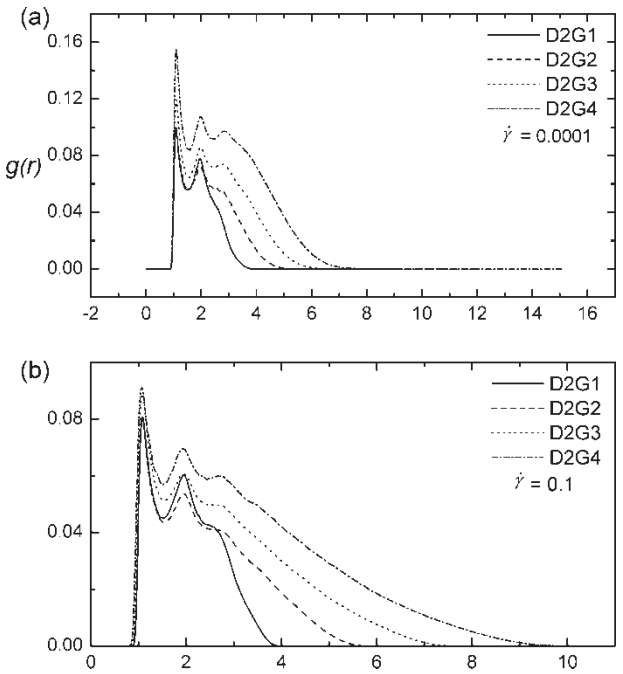


Figure 3. Radial distribution function of the terminal groups of our dendrimer systems with reference to the central unit. (a) at a weak strain rate of $\dot{\gamma} = 10^{-4}$, (b) at a higher strain rate of $\dot{\gamma} = 0.1$. Figure reproduced with permission from [1].

computing the radial distribution function of the terminal groups with reference to the central unit:

$$g(r) = \frac{\left\langle \sum_{i=0}^{N_m} \sum_{\alpha} \delta(r - |\mathbf{r}_{i\alpha} - \mathbf{r}_{i1}|) \right\rangle}{4\pi r^2 N_m} \tag{7}$$

where $\mathbf{r}_{i1}$ is the position of the core, $\alpha$ runs over all terminal groups of the dendrimer, and $N_m$ is the number of molecules. This is shown in figure 3 for dendrimers at relatively weak (a) and strong (b) strain rates. In each case the end groups are found everywhere throughout the interior of the molecule, in agreement with experimentally observed back folding of branches by Scherrenberg *et al.* [10]. It is this back folding of terminal branches that assists in suppressing the entanglement of dendrimers.

Further evidence for the lack of entanglement in dendrimers can be seen in figure 4, which shows a plot of the zero-shear viscosity (defined as $\eta_0 = \lim_{\dot{\gamma}\to 0} \eta$) vs molecular weight ($M$) for our model dendrimer melts and corresponding model linear polymers of the same molecular weight. In the case of linear polymers we observe the classic Rouse behaviour [11], wherein for low molecular weight chains where chain entanglement is minimal, $\eta_0 \propto M$. At higher molecular weights chain entanglement dominates the dynamics and molecules move along their own backbones. This is known as reptation dynamics [12]. In this case we notice a sharp change in slope at approximately $M = 100$, where $\eta_0 \propto M^{\nu}$, and the exponent takes on a value $\nu > 3$. On the other hand, dendrimers display no characteristic change in

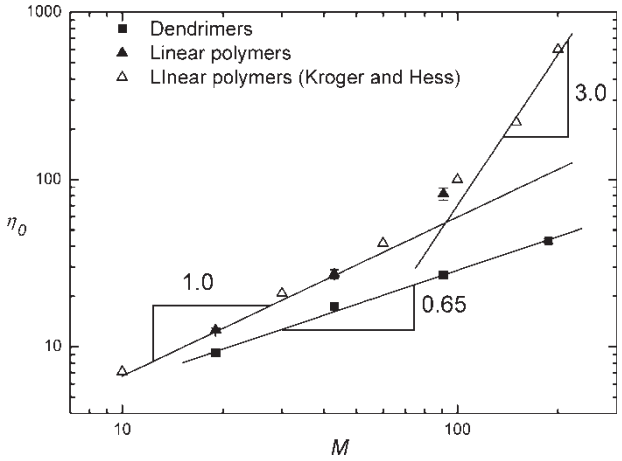


Figure 4. Zero shear viscosity as a function of molecular mass for our dendrimer and linear polymer models. Also shown is data for linear polymers taken from Kröger and Hess [13]. Figure reproduced with permission from [2].

slope. For all generations studied, our model dendrimers obey a single power law, $\eta_0 \propto M^{0.65}$. In all cases the zero shear viscosity of a dendrimer melt is significantly less than the zero-shear viscosity of a linear polymer of the same molecular weight. This is a direct result of the compact spherical molecular structure and nonentanglement of terminal end groups, due to their back folding, as displayed in figure 3.

A plot of the radius of gyration against molecular weight reveals a power law behaviour for all dendrimers studied. A fractal dimension may be defined as $d_f = 1/v$, where $v$ is the slope of a log–log plot of $R_g$ vs $M$. $d_f$ can be computed for dendrimers at equilibrium and as a function of strain rate and is found to vary from a maximum of $\sim 3$ at equilibrium down to average values of $\sim 2.5$ at strain rates of 0.1 [1]. A value of $d_f \sim 3$ at equilibrium indicates that the structure of dendrimers is highly compact, filling essentially all the space available to it. As strain rate increases, spherical symmetry is destroyed and dendrimers stretch out more, leaving gaps in the available space and hence reducing their fractal dimension.

The rheological properties of dendrimers may be compared to linear polymers of equivalent molecular weight. In figure 5 the shear viscosity is shown as a function of strain rate for dendrimers and linear chains. All of the systems exhibit the transition from the Newtonian regime for small strain rates to the non-Newtonian regime for high strain rates. The flow curves can be characterized by the zero-shear viscosity and the value of an exponent in the power-law region $\eta \propto \dot{\gamma}^{-n}$. The exponents in the power-law region of the $\eta$ vs $\dot{\gamma}$ relationship in the case of both dendrimers and linear polymers increase with molecular mass, but the increase is more rapid for linear polymers. The absolute values of the exponents are also larger for linear chain molecules. This is in contrast with recent results reported by Kröger and Hess [13] who find invariant exponents, and possible reasons for this are discussed in [2].

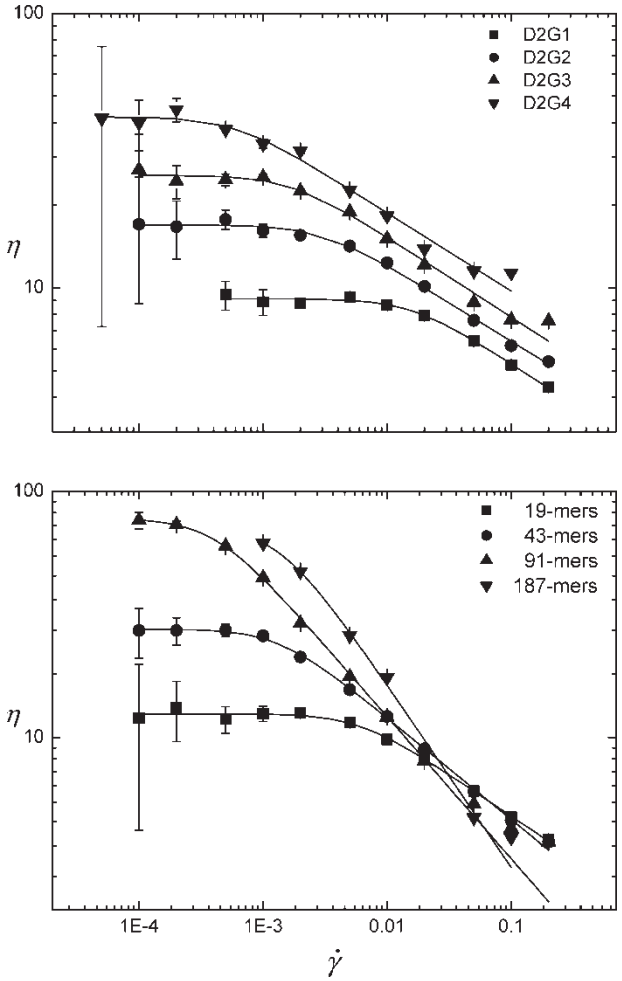


Figure 5. Shear viscosity as a function of strain rate for dendrimers of generation 1–4 and linear polymers of the same molecular weight. Figure reproduced with permission from [2].

Direct comparison of the viscosity–strain rate curves for dendrimers with those of traditional linear chain polymers of the same size (at the same density and temperature) show that when the fluid is in the Newtonian regime the viscosity of dendrimer melts is always lower than that of the linear molecules. Back folding of end branches and the compact geometrical structure of dendrimers together inhibit intermolecular entanglement, resulting in a decrease in viscosity. In the non-Newtonian regime the exponent in the power law region is always smaller for dendrimer melts in comparison to linear chain polymers, leading to lower viscosities for linear chains in comparison to dendrimers of the same molecular weight. Now the branching of dendrimers limits both shear-induced the alignment of molecules leading to a slow-down in shear deformation and thinning. This behaviour is consistent with the earlier conclusions drawn from the analysis of the eigenvalues of the radius of gyration tensor.

One may also compute the birefringence angle $\chi$ as the angle between the flow direction and the alignment direction, the order parameter $S$ which varies from 0 (in the case of orientational disorder) to 1 (for perfect alignment), and the spin angular velocity [2]. For both

linear chains and dendrimers the alignment angle decreases with increasing strain rate, whereas for small strain rates it converges to 45°(expected in the Newtonian regime). The alignment angle is always smaller for linear chains than for dendrimers of the same molecular mass, whereas the order parameter is higher for linear chains than for dendrimers. This expresses the fact that for equivalent strain rates linear chains more easily stretch and align with respect to the flow field than dendrimers of the same molecular weight, a consequence of the compact and constraint-limiting geometry of dendrimer molecules compared to the more open and less constrained linear molecules. The spin angular velocity of dendrimers has also been computed [2] and seems not to depend on the molecular mass (generation). The slope of a plot of angular velocity vs strain rate converges to the theoretical value of $-1/2$ at higher values of $\dot{\gamma}$ than for linear chain molecules. Moreover in the case of chain molecules, the rotation is strongly correlated with the chain length. The relative ease of rotation of dendrimers is a direct consequence of the compact and symmetric dendrimer architecture that prevents branch entanglement.

More detailed discussion of these results and others including the distribution of terminal end groups, structural analysis of dendrimers under shear and normal stress coefficients is given in [1,2]. Further work on NEMD simulations of solutions of dendrimers and blends of polymer/dendrimer systems will be published shortly.



## 3. The Arnold cat map and elongational flow

### 3.1 Introduction

Until very recently it was thought that dynamical simulations of planar elongational flow using NEMD were impossible to perform for molecular systems because the unit cell is compressed in at least one of the flow directions. This constraint demands that simulations cease once the length of the cell in the contracting direction reaches its minimum possible extent of twice the range of the interatomic potential radius. For molecular fluids, such as polymer melts, steady-state cannot be achieved because the characteristic relaxation times are significantly larger than the time taken to reach the minimum extension of the simulation cell. This was a severe limitation for microscopic dynamical simulations, because elongational flow is in many ways more significant for the rheology of polymer materials than shear flow, which is relatively straightforward to simulate using standard NEMD techniques.

Over a decade ago, Kraynik and Reinelt [14] found a set of elongating lattices that were periodic in space after a time $\tau_p$. It was later demonstrated [15–17] that the cells of these lattices could be used as the boundaries for simulation cells of a homogeneous NEMD simulation of planar elongational flow. These boundaries are periodic in both space and time. Their spatial periodicity ensures the system remains homogeneous, whereas the temporal periodicity allows NEMD simulations of unrestricted duration. This in turn has allowed the first simulations of long-chain polymer melts undergoing steady-state planar elongational flow [18].

Recently we discovered [19] that the lattices found by Kraynik and Reinelt are closely related to the Arnold cat map [20], which is a simple area preserving map of the torus onto itself that has been studied extensively in the dynamical systems literature as a case example of a strongly chaotic system of low dimension. We showed how application of the cat map greatly simplifies the derivation of the eigenvalues and eigenvectors of the lattices computed by Kraynik and Reinelt, as well as the alignment angles that such a spatio-temporally periodic simulation cell makes with respect to the flow fields. In what follows, this connection is reviewed and some new insights into the nature of elongational flow are presented.

### 3.2 Dynamical maps and periodic boundary conditions

In MD simulations the time evolution of the positions and momenta of a system of atoms or molecules is calculated by numerically integrating the governing equations of motion. However fluid systems are almost never at equilibrium. One of the objectives of NEMD has been to simulate systems of atoms and molecules with constant shear or elongation gradients. Homogeneous flows with such flow fields are only possible with suitable periodic boundary conditions that are compatible with the flow geometry.

An equilibrium MD simulation at constant energy is readily implemented by integrating Newton's equations of motion for the time evolution of positions and momenta. One may simulate other ensembles, e.g., $(N, V, T)$, $(N, p, T)$, etc., by suitable perturbations to the equations of motion that involve the introduction of thermostats, barostats, etc. For the system to remain homogeneous in space one applies standard periodic boundary conditions used in MD. What is not as well known is that these boundary conditions are equivalent to spatio-temporal mappings.

A dynamical map is an operation that transforms the state of a system at time $t$ to an allowable state at time $t+1$. Maps have been particularly instrumental in our understanding of chaos in dynamical systems in recent years. A functional mapping may be defined as

$$\mathbf{x}_{t+1} = \mathbf{M}(\mathbf{x}_t) \tag{8}$$

where $\mathbf{x}$ is an $n$-dimensional vector that describes the state of the system and $\mathbf{M}$ is the mapping operation. For the case of an equilibrium MD system, such a mapping scheme for particle positions is shown in figure 6 and expressed mathematically as

$$\begin{pmatrix} x' \\ y' \\ z' \end{pmatrix} = \begin{pmatrix} 1 & 0 & 0 \\ 0 & 1 & 0 \\ 0 & 0 & 1 \end{pmatrix} \begin{pmatrix} x \\ y \\ z \end{pmatrix} \bmod (L) \tag{9}$$

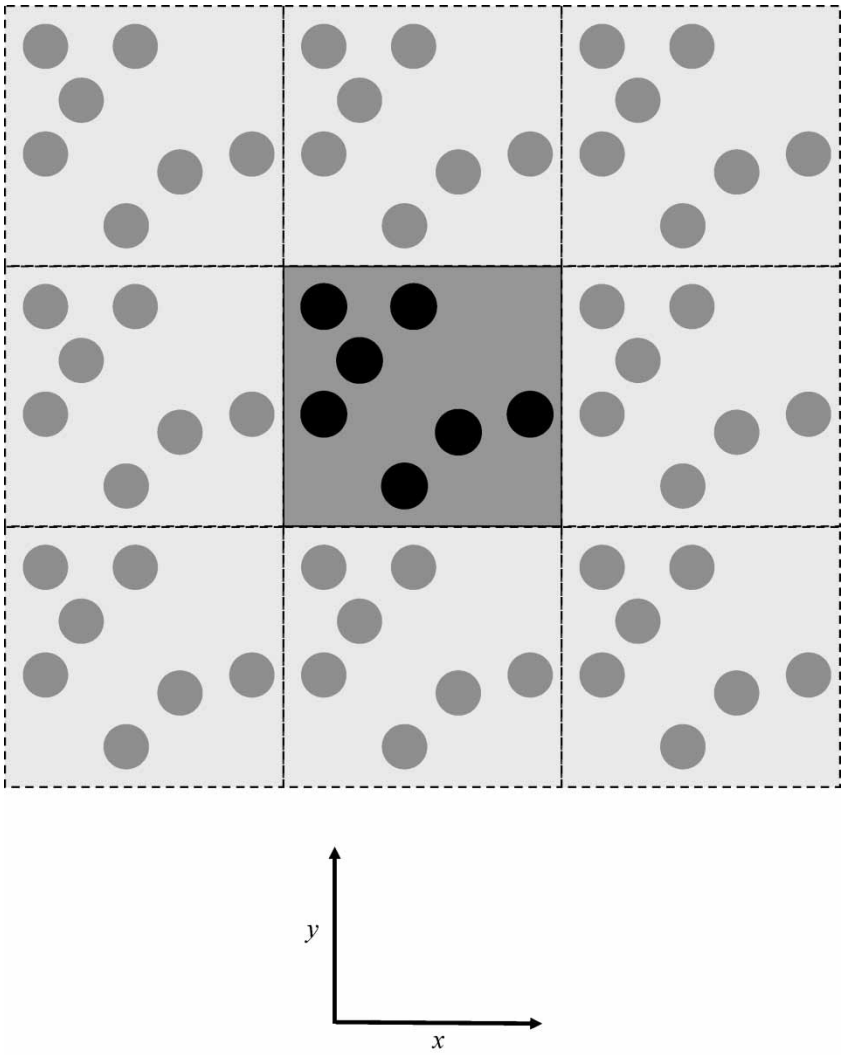


Figure 6. Two dimensional representation of periodic boundary conditions for a system of atoms at equilibrium. The central square represents the simulation box. All other boxes are periodic images of this central one.

where $L$ is the length of the simulation cell. The physical mapping of a particle with coordinates $\mathbf{x} = (x, y, z)$ into one with coordinates $\mathbf{x}' = (x', y', z')$ occurs due to the modulo operation. The mapping operation shown in equation (9) is thus equivalent to the scheme of periodic boundary conditions used in typical equilibrium MD simulations. It says that a particle inside the simulation box stays inside the box. If it moves outside the box in any direction, then it is placed back inside the box by a translation of length $L$ in that direction.

For planar shear flow (fluid flowing in the $x$-direction with constant velocity gradient in the $y$-direction) the mapping scheme is given as

$$\begin{pmatrix} x' \\ y' \\ z' \end{pmatrix} = \begin{pmatrix} 1 & \dot{\gamma}t & 0 \\ 0 & 1 & 0 \\ 0 & 0 & 1 \end{pmatrix} \begin{pmatrix} x \\ y \\ z \end{pmatrix} \bmod (L) \qquad (10)$$

where $\dot{\gamma} = \partial u_x / \partial y$ is the strain rate. Now in addition to simple translations of a particle's position if it moves out of the left or right cell boundaries, one must account for the effects of the convective flow as a particle moves out of the top or bottom boundaries. In this case the $x$-position of the particle is shifted by an amount $\pm \dot{\gamma} L \Delta t$, where $\Delta t$ is the integration time step, if the particle moves out of the bottom or top boundary, respectively.

Viewed from this perspective, the maps described by Eqs. (9) and (10) represent the *convective* component of the fluid's flow. They tell us absolutely nothing about the thermal motion of atoms within the fluid which, for homogeneous flow, evolve under appropriate equations of motion, such as the SLLOD equations [6]. Rather, they tell us how a volume of fluid deforms as time advances. At equilibrium there is no convective flow and so the simulation cell remains cubic. For shear flow the cell deforms with the flow, starting out as a cube and evolving into a three-dimensional rhomboid. However, at times $t = \tau_p = \dot{\gamma}^{-1}$ it can be shown that the cell is periodic in space [6]. This allows one to map the deformed rhomboid back into the original cubic cell without any discontinuity, as shown in figure 7. While such a periodicity does imply that homogeneous simulations of planar shear flow are

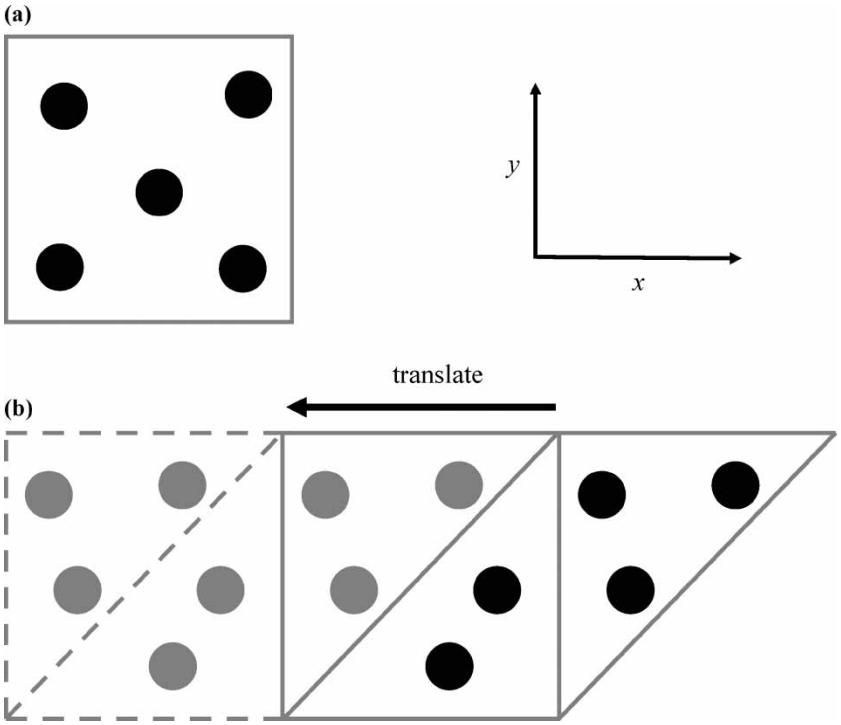


Figure 7. Simulation cell at (a) equilibrium and (b) under planar shear represented in two dimensions. In (b) the box (depicted by solid lines encapsulating black atoms) deforms into a rhomboid. By translating the right half of the deformed box by the length of the box in the $x$-direction, one can map the deformed box back into the original square shape. The equivalence of both boundary conditions is seen by comparison of the relative positions of all atoms and their images (enclosed by dashed boundaries), which remain preserved under the mapping.



nonautonomous in nature, the effects of the periodicity are only observable in systems of very few numbers of particles [21] and are unobservable in systems of practical interest. Note that the elimination of discontinuities in the flow can only be achieved with an appropriate coupling of the equations of motion to the system's periodic boundary conditions. For homogeneous shear flow the most commonly used combination are the SLLOD equations of motion [6] and Lees–Edwards boundary conditions [7].

In the case of planar elongational flow the mapping scheme for particle positions is given by

$$\begin{pmatrix} x' \\ y' \\ z' \end{pmatrix} = \begin{pmatrix} \exp(\dot{\varepsilon}t) & 0 & 0 \\ 0 & \exp(-\dot{\varepsilon}t) & 0 \\ 0 & 0 & 1 \end{pmatrix} \times \begin{pmatrix} x_0 \\ y_0 \\ z_0 \end{pmatrix} \bmod \begin{pmatrix} L_x \\ L_y \\ L_z \end{pmatrix} \tag{11}$$

where it is taken that the fluid expands in the $x$-direction at a rate $\dot{\varepsilon}$ and contracts in the $y$-direction at the same rate. $L_x$, $L_y$ and $L_z$ are the dimensions of the box in the $x$, $y$ and $z$ directions, respectively. This mapping scheme is schematically shown in figure 8. As the flow is incompressible, the flow geometry now demands that exponential expansion occurs in the $x$-direction and exponential contraction occurs in the $y$-direction. No flow takes place in the $z$-direction. This poses the serious previously mentioned problem, that such a flow via MD is doomed to extinction since the flow must cease when the length in the contracting direction ($L_y$) reaches its minimum possible value of twice the effective interaction potential radius ($r_c$). This implies a maximum simulation time of $t_{\max} = (1/\dot{\varepsilon})\ln(2r_c/L_y)$, [22] which may be significantly less than typical relaxation times of molecular fluids.

The SLLOD equations of motion may again be used [15–17,22,23] to simulate elongational flow. At around the time these first simulations were performed, it was suggested that the SLLOD equations of motion were unsuitable for elongational flow, and modified equations (GSLLOD) were proposed [24]. However, the GSLLOD equations were criticized for producing an incorrect nonequilibrium distribution function [25]. One can also readily show that it predicts the wrong energy dissipation rate. The SLLOD equations predict the correct dissipation rate as $\dot{H}_{\mathrm{SLLOD}} = -\nabla\mathbf{u} : \mathbf{P}V = -\dot{\varepsilon}(P_{xx} - P_{yy})V$ (here we assume no flow in $z$). In contrast, GSLLOD predicts an additional unphysical term quadratic in the field strength,

$$\dot{H}_{\mathrm{GSLLOD}} = \dot{H}_{\mathrm{SLLOD}} - \dot{\varepsilon}^2 \sum_{i=1}^{N} \frac{1}{m_i}(x_i p_{xi} + y_i p_{yi}).$$

As with shear flow, the SLLOD equations of motion must be coupled with appropriate periodic boundary conditions. Kraynik and Reinelt [14] demonstrated how the extensional motion of spatially periodic lattices could be generated by suitable geometric orientations of the axes of the lattice with respect to the orientation of the elongating

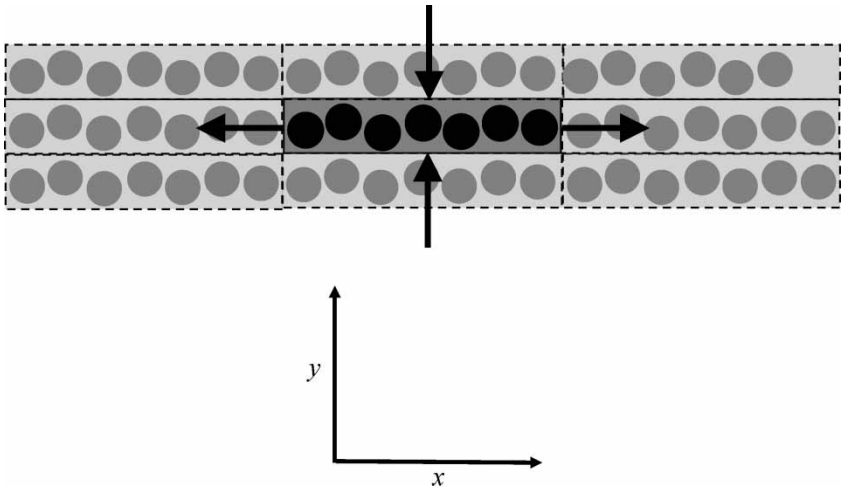


Figure 8. Conventional periodic boundary conditions for planar elongational flow in two dimensions. The simulation cell is the central rectangle with atoms shaded black. Periodic images (shaded lighter grey) surround the cell in all directions. Expansion is in the $x$-direction and contraction in the $y$-direction.



field. As described in [15–17] such periodic lattices may be used as the boundaries of a periodic simulation cell. The original derivation of the eigenvalues, eigenvectors and orientation angles required to specify these periodic boundary conditions, while complete, is algebraically involved. It forms six pages of Kraynik and Reinelt's paper, which corresponds to about a dozen A4 pages of hand-written algebraic derivation! In what follows it is shown how these periodic lattices are directly related to the Arnold cat map, and how a simplified approach to computing the eigenvalues, eigenvectors and orientation angles may be formulated.

### *3.3 The Arnold cat map and Kraynik–Reinelt boundary conditions*

The usual Arnold cat map is a map of the torus $\mathbb{T}^2 = \mathbb{R}^2/\mathbb{Z}^2$ onto itself

$$\begin{pmatrix} x' \\ y' \end{pmatrix} = \begin{pmatrix} 1 & 1 \\ 1 & 2 \end{pmatrix} \begin{pmatrix} x \\ y \end{pmatrix} \text{mod}(1). \tag{12}$$

In this representation of the cat map, expansion takes place in the eigendirection $\mathbf{e}_1$ and contraction occurs in the eigendirection $\mathbf{e}_2$ (see figure 9). Thus the cat map "flow" geometry is the opposite of the flow geometry employed by Kraynik and Reinelt and subsequent NEMD simulations of planar elongational flow [15–17]. While the flow is in two dimensions, the actual simulation cell is fully three-dimensional (no flow takes place in the $z$ direction).

The map described by equation (12) has two eigenvalues,

$$\lambda_1 = \frac{3 + 5^{1/2}}{2} > 1 \quad \text{and} \qquad \lambda_1^{-1} = \lambda_2 = \frac{3 - 5^{1/2}}{2} < 1. \tag{13}$$

These eigenvalues are equivalent to those found by Kraynik and Reinelt. For the cat map, this corresponds to an alignment of the direction of expansion (in this case, parallel to the eigenvector $\mathbf{e}_1$), at an angle of $\theta = 31.7°$ with respect to the $y$-axis (equivalent to the angle formed between $\mathbf{e}_2$ and the $x$-axis). Since the map is area preserving, the product of any set of eigenvalue pairs is 1. The eigenvectors of the map described by equation (12) are

$$\mathbf{e}_1 = \begin{pmatrix} s \\ \frac{5^{1/2}+1}{2} s \end{pmatrix} \quad \text{and} \quad \mathbf{e}_2 = \begin{pmatrix} s \\ \frac{-5^{1/2}+1}{2} s \end{pmatrix} \tag{14}$$

where $s$ is a real number. $s = 1$ is used for convenience.

We note here that the Arnold cat map transformation is equivalent to the mapping that takes place in the Kraynik–Reinelt lattice when the Hencky strain, $\varepsilon_p = \dot{\varepsilon}\tau_p$, is attained, and it is this mapping which makes the Kraynik–Reinelt system reproducible and hence periodic in time as well as space.

In figure 9 the map is illustrated in a manner familiar to physicists since the days of Schrödinger, who for some reason seem to have a vendetta against the feline co-inhabitants of our planet. In figure 9(a) a cat sits happy and content. But not for long. After one application of the map figure 9(b), the cat is stretched along $\mathbf{e}_1$, compressed along $\mathbf{e}_2$, and folded back into the unit cell via the modulo operation. This stretching, compressing and folding (mapping) operation is repeated for the next two iterations in figure 9(c) and figure 9(d). As is evident, our poor cat is somewhat disoriented and rather chaotic at this stage. It is this chaotic feature that has made Arnold's cat almost as famous as Schrödinger's!

Now, there is something very interesting and very useful about the cat map and its relationship to planar elongational flow. In figure 10(a) the cat map is shown after the mapping operation described by equation (12) (i.e., after stretching and contraction takes place) but

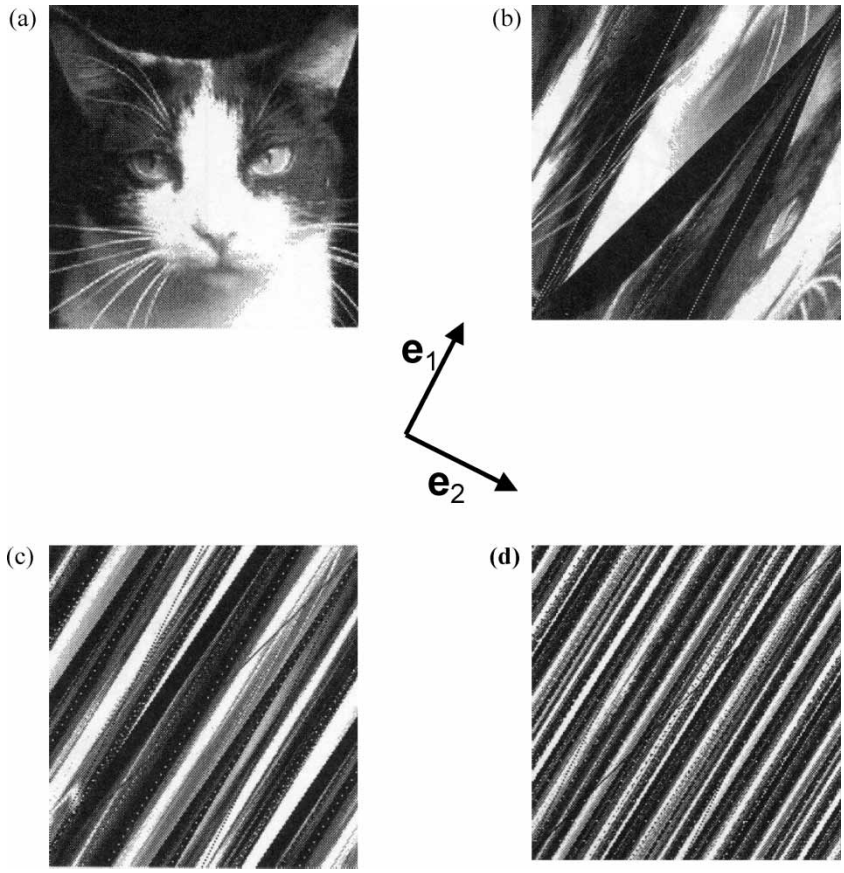


Figure 9. The Arnold cat map. (a) Unperturbed cat. The cat is thereafter shown after (b) one, (c) two and (d) three iterations of the map. Figure reproduced with permission from [37].



*before* the modulo operation (i.e., before folding back into the unit cell). In this diagram various parts of the cell are represented by different symbols (diamonds, squares, circles and triangles) to more clearly demonstrate how the folding operation occurs. With application of the modulo operation folding takes place, and the elongated cell is mapped back into the unit cell as shown in figure 10(b). It is clear from figure 10(b) how the different regions of the elongated cell are mapped back into the unit square. In figure 10(c) the elongated cell in figure 10(a) is again shown, but this time replicated with periodic images of itself. What is both remarkable and highly instructive about this representation is that the periodic images that appear in the original unit cell *exactly* match the sections of the original elongated cell that are physically mapped back into the unit square by the modulo operation shown in figure 10(b). What this means is that the modulo operation of the cat map is *equivalent* to alignment of the elongated cell with infinite periodic images of itself. But this is exactly the "trick" one uses to simulate indefinite planar shear flow by NEMD: an infinite periodic system that is deformed in space is appropriately mapped back into a more compact geometry by an operation that is periodic in time. Thus the cat map can be used as periodic boundary conditions for indefinite elongational flow in much the same way that Lees–Edwards boundary conditions can be used as the boundary conditions for planar shear flow! In fact, several years before the connection with the cat map was made, Todd and Daivis [16] showed how similar the boundary conditions for planar elongation and planar shear really are.

The example given in equation (12) is not a unique example of this type of map. In fact there are an infinite number of "cat maps" each with only three constraints: the matrix must be symmetric, have integer elements, and unit determinant (i.e., it must be area preserving). These maps are known collectively as hyperbolic toral automorphisms, which in turn are a set of Anosov diffeomorphisms [26]. The family of lattices found by Kraynik and Reinelt [14] corresponds to a subset of hyperbolic toral automorphisms.

Hunt and Todd [19] showed that it is far simpler to compute the eigenvalues, eigenvectors and orientation angles from the cat map formalism, rather than the method employed by Kraynik and Reinelt [14]. Consider the set of Anosov diffeomorphisms with the mapping

$$\mathbf{x}_{t+1} = \mathbf{M}(\mathbf{x}_t) \tag{15}$$

where

$$\mathbf{M} = \begin{pmatrix} m_1 & m_2 \\ m_2 & m_3 \end{pmatrix} \tag{16}$$

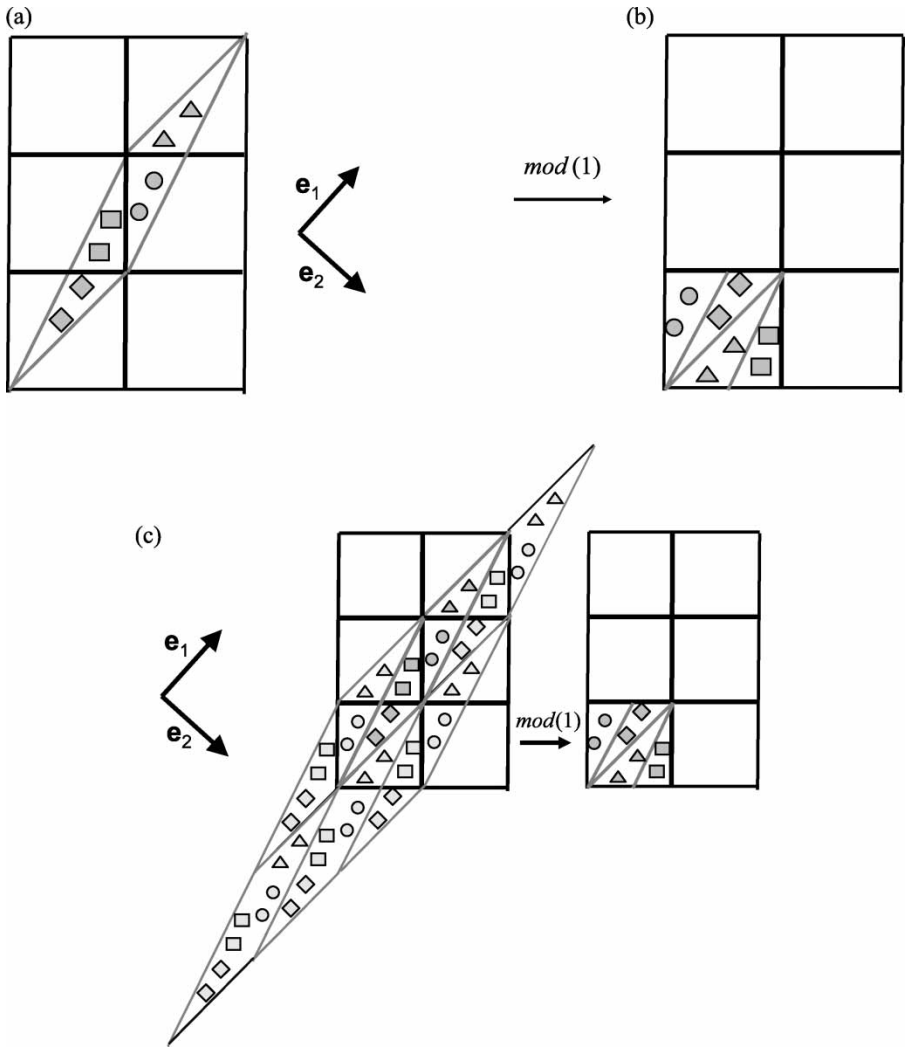




Figure 10. (a) The cat map after stretching along $\mathbf{e}_1$ and contraction along $\mathbf{e}_2$ but before the modulo operation. Different regions of the map are drawn with different symbols to aid visualization of the modulo (i.e., folding) operation. (b) After the modulo operation. (c) Equivalence of the modulo operation with infinite periodic images of the elongated cell in (a).

is symmetric, $m_1$, $m_2$, $m_3 \in \mathbb{Z}$ and

$$\det(\mathbf{M}) = m_1 m_3 - m_2^2 = 1. \tag{17}$$

The eigenvalue equation for the map described by equation (16) is

$$\det(\lambda \mathbf{l} - \mathbf{M}) = 0 \tag{18}$$

which, when solved substituting in equation (17) for $\det(\mathbf{M}) = 1$, gives the pair of eigenvalues

$$\lambda = \frac{(m_1 + m_3) \pm \left[(m_1 + m_3)^2 - 4\right]^{1/2}}{2}. \tag{19}$$

The Hencky strain is simply computed as $\varepsilon_p = \ln(\lambda)$ [14]. Of interest, the Hencky strain is equivalent to the Lyapunov exponent for the cat map! It is both that value of strain at which the simulation cell can be mapped back into the original square and the product of the rate of exponential divergence of neighbouring regions of phase space with the mapping iteration time (in this case, unity).

The eigenvectors of $\mathbf{M}$ may now be trivially computed from the set of linear equations

$$\mathbf{M}\mathbf{x} = \lambda \mathbf{x} \tag{20}$$

giving

$$\mathbf{e}_1 = \begin{pmatrix} s \\ \frac{(\lambda_1 - m_1)}{m_2} s \end{pmatrix} \quad \text{and} \quad \mathbf{e}_2 = \begin{pmatrix} s \\ \frac{(\lambda_2 - m_1)}{m_2} s \end{pmatrix}. \tag{21}$$

Again $s = 1$ is used for convenience. Note that $m_2 = 0$ does not correspond to an Anosov diffeomorphism.

If we define the unit vector in the $y$-direction as $\hat{\mathbf{y}}$, then the orientation angle (i.e., the angle between the expanding direction and the $y$-axis) can be thus simply computed from

$$\mathbf{e}_1 \cdot \hat{\mathbf{y}} = \|\mathbf{e}_1\| \, \|\hat{\mathbf{y}}\| \cos\theta \tag{22}$$

that is,

$$\theta = \cos^{-1}\left(\frac{1}{\|\mathbf{e}_1\|}\right). \tag{23}$$

Our derivation of the eigenvalues, eigenvectors and orientation angles is somewhat more straightforward and simpler to that worked out in [14], taking only several lines of simple algebra. In particular, it is the orientation angle and Hencky strain/Lyapunov exponent (hence, strain period) that are of central importance in the practical implementation of the K–R map in NEMD simulations [15,16].

As an example, consider the map

$$\mathbf{M} = \begin{pmatrix} 5 & 2 \\ 2 & 1 \end{pmatrix}.$$

It has eigenvalues $\lambda = 3 \pm 2.2^{1/2}$ and eigenvectors

$$\mathbf{e}_1 = \begin{pmatrix} 1 \\ -1 + 2^{1/2} \end{pmatrix} \quad \text{and} \quad \mathbf{e}_2 = \begin{pmatrix} 1 \\ -1 - 2^{1/2} \end{pmatrix}.$$

The Hencky strain/Lyapunov exponent ($\ln \lambda$) is 1.76275 and the orientation angle (from equation (23)) is $\theta = 22.5°$. Use of the cat map formalism determines these required quantities in several lines of trivial algebra, compared to pages of algebra following the Kraynik–Reinelt procedure.

In figure 11, it is demonstrated how useful the cat map can be in the study of a very practical problem: the simulation of polymer melts under planar elongational flow. In figure 11(a) simulation data from Daivis *et al.* [18], is presented for linear chain molecules of 20 "beads" per chain. These simulations were performed by NEMD using the K–R/cat map boundary conditions to simulate for very long times—much longer than the relaxation times of the melt, and long enough to ensure excellent statistics for all computed properties. The viscosities plotted against strain rate are therefore genuine steady-state viscosities which would not have been possible to compute using the standard rectangular periodic boundary conditions defined by equation (11). The viscosity profile demonstrates a Newtonian region at low elongation rate

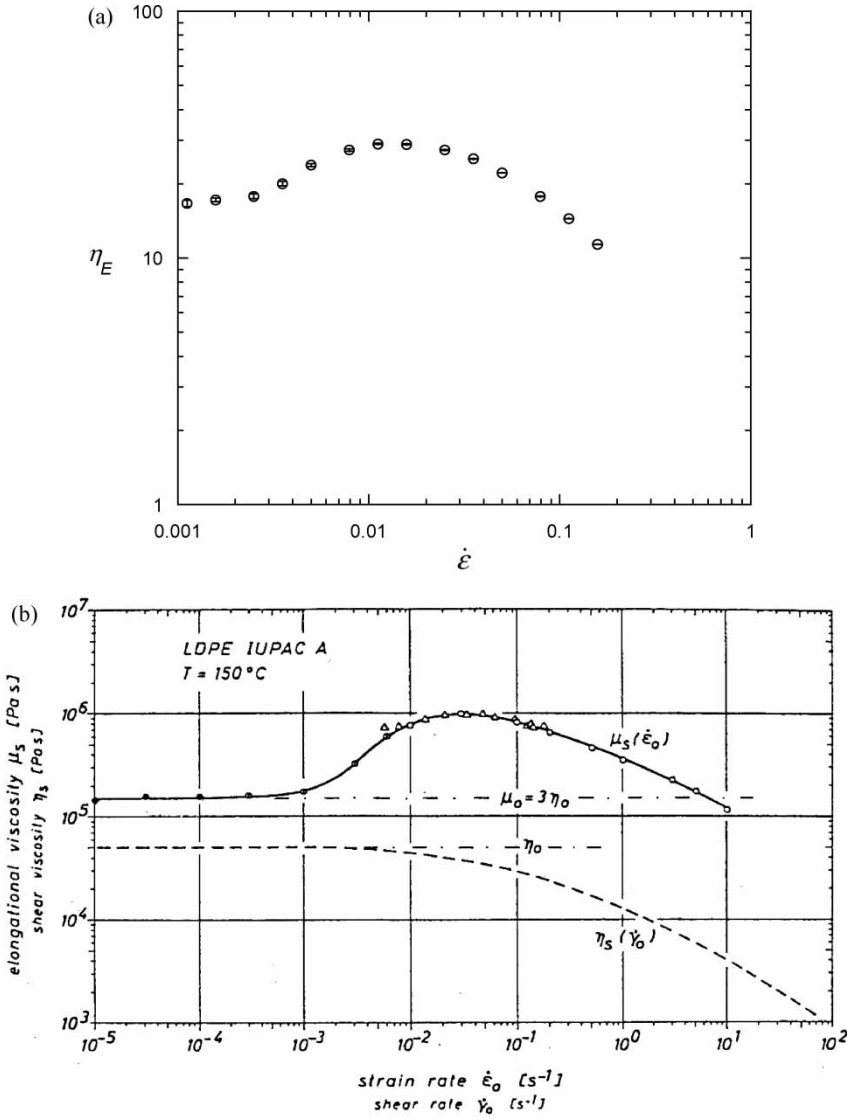


Figure 11. Elongational viscosity as a function of elongation rate for (a) an NEMD simulation of a system of freely-jointed linear chain molecules of 20 beads per chain (from Daivis *et al.*, [18]). (b) Experimentally measured elongational viscosities for a low density polyethylene melt (reproduced with permission from [27]).

(viscosity independent of strain rate), followed by an initial non-Newtonian region of strain hardening, where the viscosity increases with strain rate as the chains stretch out with the flow. After a maximum in the profile is reached the viscosity decreases with strain rate. In this region the chains are stretched out and align with the velocity streamlines, thus flowing more easily. In figure 11(b) experimental elongational viscosity data for low density polyethylene taken from Laun and Münstedt [27] is displayed. It is clear from this comparison that our NEMD simulations are in excellent qualitative agreement with the experimental results of a real polymer melt. The challenge that awaits further research in this field is to quantitatively map NEMD simulations for elongational flow onto experiment, and use these mapping schemes to quantitatively predict the viscoelastic properties of arbitrary molecular architectures.

An interesting observation about the nature of elongational flow may now be made. In earlier work Todd and Daivis [28] had shown that NEMD simulations of elongational flow were inherently unstable. The exponential growth in round-off error means that the total linear momentum of the system is not conserved; after a long time the system becomes unstable and the simulation fails catastrophically. They corrected for this numerical problem by simple procedures involving either a dynamical constraint mechanism to ensure zero total linear momentum or rescaling the momenta of all particles at every timestep such that their sum remains zero. At the time they were unaware of the link between their algorithm and the cat map. The cat map has been long favoured as a system for studying ergodicity for low dimensional dynamical systems because it is highly chaotic. The degree of its chaoticity is measured by its large positive Lyapunov exponent, defined as the rate of exponential divergence of initially close neighbouring trajectories in phase space. As discussed earlier, the mapping scheme for periodic boundary conditions can be viewed as the convectional component of a fluid's flow. The Lyapunov exponent computed for the cat map thus refers only to the convectional flow. It does not tell us anything about the $2dN$ Lyapunov exponents for a system of $N$ interacting particles in $d$ dimensions. These positive Lyapunov exponents, indicating microscopic chaotic behaviour, exist for systems both at equilibrium and under shear. However, these systems have *zero* Lyapunov exponent for the convectional component of their flow! It is therefore possible that a system of particles undergoing elongational flow will be *more* chaotic than systems at equilibrium or under shear since they will already have a strongly chaotic convectional component to them. This may be the microscopic origin of the rheological instability in polymer solutions and melts subject to elongational flow. Experimental measurements of their viscoelastic and thermophysical properties are difficult to perform at least partly for this reason. We are investigating this interesting phenomenon further.

## 4. Inhomogeneous flow and nanofluidics

### *4.1 Classical Navier–Stokes formulation for momentum transport*

There are three basic equations of motion that underpin the entire science of fluid dynamics: the continuity equations of mass, momentum and energy. Like all fundamental laws of nature, these equations express conservation principles: that the total mass, momentum or energy of a system must be equal to the sum of their input and output sources. For example, one may write the conservation of momentum principle for a single-component fluid as

$$\rho(\mathbf{r},t)\frac{\mathrm{d}\mathbf{u}(\mathbf{r},t)}{\mathrm{d}t} = -\nabla\cdot\mathbf{P}(\mathbf{r},t) + \rho(\mathbf{r},t)\mathbf{F}_e \qquad (24)$$

where $\rho(\mathbf{r},t)$, $\mathbf{u}(\mathbf{r},t)$, $\mathbf{P}(\mathbf{r},t)$ are the density, streaming velocity and pressure tensor respectively of the fluid at position $\mathbf{r}$ and time $t$ and $\mathbf{F}_e$ is an external force per unit mass. Equation (24) says that the total force per unit volume acting on a fluid is equal to the sum of the internal forces per unit volume ($-\nabla\cdot\mathbf{P}(\mathbf{r},t)$) and the external forces per unit volume ($\rho(\mathbf{r},t)\mathbf{F}_e$).

Equation (24) is completely general for any single component fluid arbitrarily far from equilibrium. In order to use equation (24) for specific problems one first needs to identify the geometrical nature of the flow. In figure 12 a diagram is presented of a fluid confined between planar walls acting under the influence of an external driving force. Such a flow is representative of gravity driven flow; it is also equivalent to planar Poiseuille flow which, though driven by a pressure gradient, is essentially indistinguishable from a flow that is driven by an external field [29]. If we assume that our fluid is in the steady-state, that the eternal force per unit mass is constant, and that our system is homogeneous in space (this would be true in the case of figure 12 if the channel separation in the $y$-direction is very large compared to the range of interatomic interactions) then equation (24) reduces to

$$\frac{\mathrm{d}P_{yx}(y)}{\mathrm{d}y} = \rho F_e \qquad (25)$$

which, when solved, yields a linear function in $y$ for the shear stress ($-P_{yx}(y)$). However, we cannot deduce the streaming

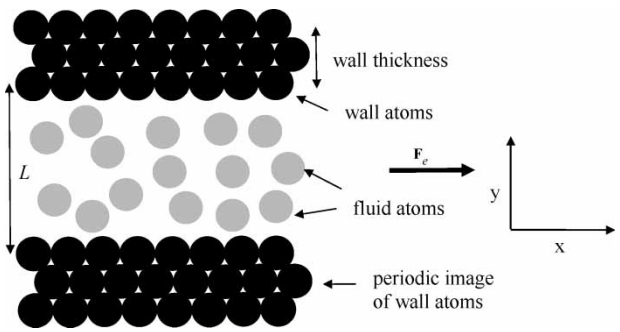


Figure 12. Geometry for planar Poiseuille flow in a narrow confined channel.

velocity profile $u_x(y)$ from this solution. In order to obtain this property one must make use of an appropriate phenomenological model, one that links a thermodynamic flux (the shear stress) with its conjugate driving thermodynamic field (the velocity gradient). The appropriate constitutive relation for momentum transfer is of course Newton's law of viscosity, $P_{yx} = -\eta\dot{\gamma}$, where $\eta$ is the shear viscosity (a material property of the fluid) and $\dot{\gamma} = \partial u_x/\partial y$ is the strain rate. Substitution of Newton's law into equation (25) and solving yields the classical Navier–Stokes solution for the velocity profile for this type of flow:

$$u_x(y) = -\frac{L^2\rho F_e}{2\eta}(\bar{y}^2 - 1) \tag{26}$$

where $L$ is the separation of the channel in the $y$-direction, $\bar{y} = y/L$, and we have assumed the boundary condition that at the walls the streaming velocity is zero.

We can test the accuracy of this prediction by conducting nonequilibrium MD simulations of a confined fluid under the influence of a constant external force. Our system consists of a simple single-component WCA fluid [5] confined between atomistic walls, also modelled by the WCA potential with an additional harmonic potential to allow vibration of atoms around their equilibrium fixed points. In our simulation the fluid and wall atoms evolve in time via Newton's equations of motion.

The walls have additional constraints to keep their temperature constant (thus acting as a sink for energy dissipation of the fluid) and to ensure that their centre of mass remains fixed. Full details of the equations of motion for fluid and wall atoms and simulation method are given elsewhere [29].

In a recent study Zhang, Todd and Travis [30] performed simulations for three different channel separations: $L = 5.1$, 10.2 and 15.3 (lengths quoted are in dimensionless reduced units). In figure 13 their simulated streaming velocity profiles for these three channel widths at two different mean fluid densities is displayed. The widest system shows excellent agreement with the Navier–Stokes prediction of a quadratic streaming velocity. This prediction gets worse as the channel width decreases. At a width of $L = 5.1$ the Navier–Stokes prediction breaks down entirely.

At first thought, one might assume that the breakdown of Navier–Stokes behaviour is entirely due to an incorrect assumption about the constancy of both the density and the viscosity used to solve equation (25). The density is clearly not constant across the fluid, as seen in figure 14. If we assume that Newton's law of viscosity is valid anywhere in the fluid, we could compute a position-dependent viscosity defined as

$$\eta(y) = -\frac{P_{yx}(y)}{\dot{\gamma}(y)}. \tag{27}$$

One may compute $P_{yx}(y)$ from our simulation by either the so-called Method of Planes technique [29] or by integrating the momentum continuity equation (equation (25)), where we now note that density is no longer

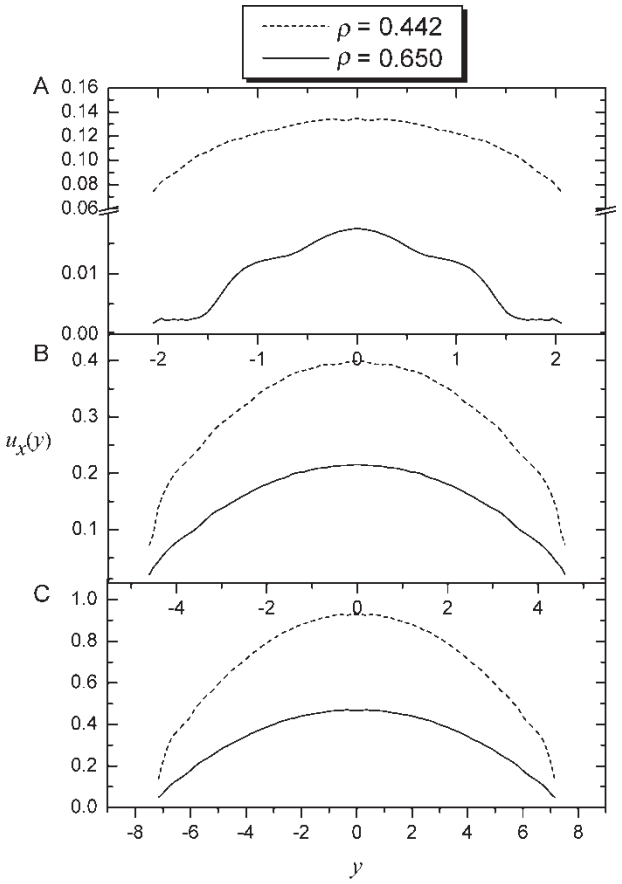


Figure 13. Streaming velocity profiles for channels of width $L = 5.1$, 10.2 and 15.3 at mean reduced densities of 0.442 and 0.65. Figure reproduced with permission from [30].

constant. The strain rate is easily obtained by numerically differentiating the velocity profiles in figure 13. The viscosity for our $L = 5.1$ ($\rho = 0.65$) system defined by equation (27) given in figure 15. However, the predicted viscosity profile is absurd! The presence of zeros in the strain rate profile in several locations within the fluid leads to singularities in the shear viscosity. In these neighbourhoods, the viscosity also becomes negative. Both features are physically unreal. There can be only one conclusion: Newton's constitutive equation for the shear viscosity must be wrong for nano-confined fluids. This in turn leads to the breakdown in Navier–Stokes behaviour in our modern world of nano-everything!

### *4.2 Post-Newton, post-Navier–Stokes formulation for momentum transport*

Newton's law of viscosity, if applied to our geometry as defined by equation (27), is a *local* constitutive law. It is Markovian in that it supposes that the viscosity of a fluid depends only on the local values of the shear stress and strain rate and knows (and needs to know) nothing about its past history or nonlocal environment. For homogeneous fluids in the steady-state this is of course true. For inhomogeneous fluids, or fluids not in the steady-state,

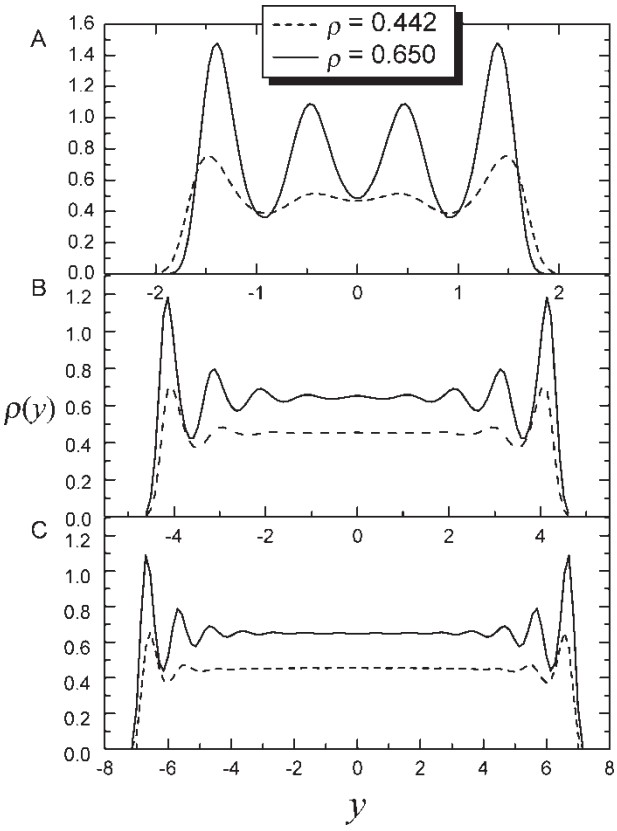


Figure 14. Density profiles for channels of width $L = 5.1$, 10.2 and 15.3 at mean reduced densities of 0.442 and 0.65. Figure reproduced with permission from [30].

Newton's law needs to be generalised to take into account non-local spatial and temporal dependencies. The most general linear constitutive relation that links the transport of momentum to a gradient in the driving thermodynamic field may be expressed as

$$P_{yx}(\mathbf{r}, t) = -\int_0^t \mathrm{d}s \int_{-\infty}^{\infty} \mathrm{d}\mathbf{r}' \eta_K(\mathbf{r} - \mathbf{r}', t - s)\dot{\gamma}(\mathbf{r}', s). \quad (28)$$

Equation (28) essentially expresses the fact that all fluids have a memory effect and therefore behave viscoelastically. These effects can only be observed if the fluid relaxation times are of the order of the experimental measurement times, or if the variations in strain rate are of the order of the range of the interatomic interactions. Both these conditions become extremely important in nanofluidics and cannot be ignored.

Equation (28), proposed by Evans and Morriss [6], has never been successfully applied to problems in nanofluidics in the past, due to a variety of technical problems [31,32]. In their recent work Zhang *et al.* [30] resolved these problems with the assumption that one ignores the explicit density dependence of the viscosity. Though not stated by Evans and Morriss [6], equation (28) is only exactly true if the fluid is homogeneous in space and only variations in the strain rate occur on molecular length-scales. For nano-confined fluids this is not the case because of large density oscillations (see figure 14). Strictly speaking, the viscosity kernel in equation (28) should be written as $\eta_K(\mathbf{r}, \mathbf{r} - \mathbf{r}', t - \mathrm{s})$, where this expresses the fact that the true nonlocal viscosity depends on where in the fluid one is, i.e., it is density dependent. By writing the kernel as $\eta_K(\mathbf{r} - \mathbf{r}', t - t')$ we compute an effective "average" viscosity. In what follows we show how to extract a meaningful effective viscosity.

Equation (28) is not terribly easy to work with. However, the whole problem can be reformulated in reciprocal space for simplicity. Zhang *et al.* [30] concern themselves only with steady-state flows, which allow one to ignore temporal dependencies. Taking the Fourier transform of equation (28) gives us

$$\tilde{P}_{xy}(\mathbf{k}) - \tilde{\eta}_K(\mathbf{k})\tilde{\dot{\gamma}}(\mathbf{k}) \quad (29)$$

where the tilde depicts the Fourier transform. The shear viscosity in momentum space may thus be obtained by simply taking the ratio of the Fourier transformed shear stress and strain rate, both obtained by numerical transforms of the real-space simulation data. A numerical inverse transform recovers the viscous kernel defined by equation (28). The viscous kernel is shown in figure 16 for our $L = 5.1$, $\rho = 0.442$ system. The kernel represents an effective nonlocal viscosity density which, when integrated over all space, gives an effective pore viscosity. Here the argument in the kernel ($y$) is interpreted as a relative distance between two points in the fluid. Thus an effective "pore viscosity" may be obtained as the only way that an exact position dependent viscosity could be

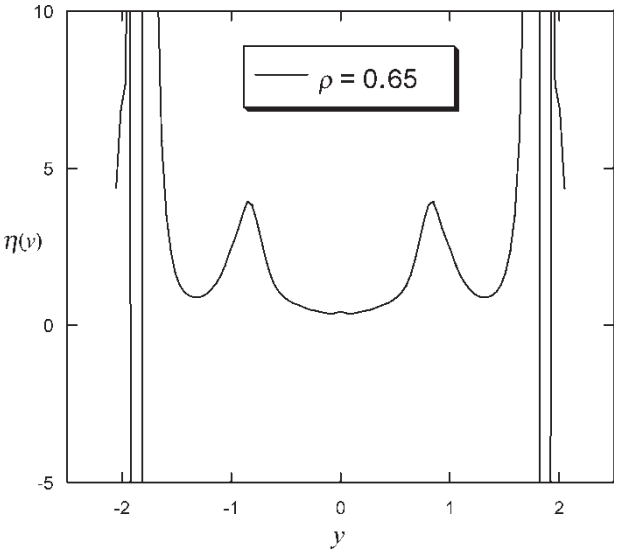


Figure 15. Local viscosity defined by Newton's law (equation (27)) for a pore of width $L = 5.1$ and mean reduced density 0.65. The singular value of the viscosity at $y = 0$ has been masked for clarity of visualisation. Data taken from [30].

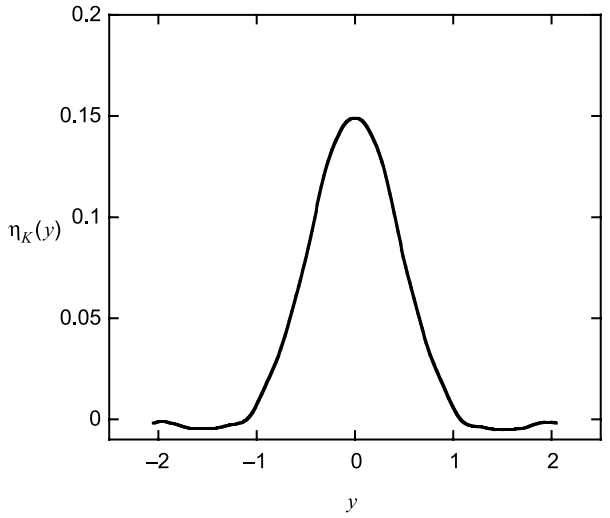


Figure 16. Non-local viscosity kernel as a function of relative position y. $\rho = 0.442$, $L = 5.1$. Data taken from [30].

determined would be to compute $\eta_K(\mathbf{r}, \mathbf{r} - \mathbf{r}')$ such that

$$\eta(\mathbf{r}) = + \int_{-\infty}^{\infty} \mathrm{d}\mathbf{r}' \eta_K(\mathbf{r}, \mathbf{r} - \mathbf{r}'). \tag{30}$$

At this stage it is not known how the extraction of $\eta_K(\mathbf{r}, \mathbf{r} - \mathbf{r}')$ can be performed from a single simulation of the type described in [30].

### *4.3 Generalised Navier–Stokes equation and prediction of flow profile*

One may generalize the Navier–Stokes equations by incorporating nonlocal constitutive equations into the continuity equations. This is most easily accomplished by working in reciprocal space. Fourier transforming equation (24) gives

$$\tilde{f}\left\{\rho(\mathbf{r}, t)\frac{\mathrm{d}\mathbf{u}(\mathbf{r}, t)}{\mathrm{d}t}\right\} = -i\mathbf{k}\cdot\tilde{\mathbf{P}}(\mathbf{k}, t) + \tilde{\rho}(\mathbf{k}, t)\mathbf{F}_e \tag{31}$$

where $\tilde{f}\{\ldots\}$ denotes the Fourier transform of the quantity in brackets and the tildes on other quantities also designate their Fourier transforms. For our field-driven time-independent flow, equation (31) reduces to

$$ik_y\tilde{P}_{yx}(k_y) = F_e\tilde{\rho}(k_y). \tag{32}$$

By the convolution rule our generalized nonlocal constitutive equation states

$$\tilde{P}_{yx}(k_y) = -\tilde{\eta}_K(k_y)\tilde{\dot{\gamma}}(k_y) \tag{33}$$

which, when substituted into equation (32), gives

$$\tilde{\dot{\gamma}}(k_y) = -\frac{F_e\tilde{\rho}(k_y)}{ik_y\tilde{\eta}_K(k_y)}. \tag{34}$$

To obtain the flow profile, one simply takes the inverse Fourier transform of equation (34) and integrates, i.e.,

$$u_x(y) = \frac{1}{2\pi}\int \mathrm{d}y \int_{-\infty}^{\infty} \mathrm{d}k_y \tilde{\dot{\gamma}}(k_y)e^{ik_y y}. \tag{35}$$

There is of course little point doing this, since we already know what the flow profile is for Poiseuille flow (see figure 13). However, by knowing what the viscosity profile is for a nano-confined fluid of a particular channel width we can now predict the flow profile of an arbitrary flow in the weak linear limit as long as we are justified in assuming that the viscosity profile in this regime will be more or less independent of the flow geometry. Outside this regime this approximation will fail as the viscosity will be a strong function of thermodynamic state point (i.e., temperature, density and strain rate), and the state point is strongly dependent on the flow geometry far from equilibrium.

Let us now try to predict an approximate flow profile of a nano-confined fluid undergoing planar Couette flow. In this example, the fluid has no external force acting upon it but is driven away from equilibrium by co-moving walls, flowing with equal and opposite constant velocities in the $x$-direction. For this geometry in the steady-state we have

$$\frac{\mathrm{d}P_{yx}(y)}{\mathrm{d}y} = 0. \tag{36}$$

For planar Couette flow, no matter how strong the density inhomogeneities are in the system, the shear stress will always have a constant value, unlike Poiseuille flow, where the shear stress demonstrates significant oscillations near the walls. In reciprocal space this becomes

$$\tilde{P}_{yx}(k_y) = 2\pi P_{yx}\delta(k_y) \tag{37}$$

where $P_{yx}$ (the shear stress) is a constant obtained by integrating equation (36). Substituting equation (33) into the left hand side of equation (37) yields

$$\tilde{\dot{\gamma}}(k_y) = -\frac{2\pi P_{yx}\delta(k_y)}{\tilde{\eta}_K(k_y)} \tag{38}$$

where we note now that the viscous kernel used in equation (38) is the one computed for Poiseuille flow, and we have used the assumption that the viscosity of a fluid undergoing Couette flow will be approximately the same as that for a fluid undergoing Poiseuille flow, in the weak flow limit. Once again, to obtain the velocity profile one takes the inverse Fourier transform of equation (38) and integrates over $y$. However, it is clear that equation (38) can only give us a linear streaming velocity profile.

To obtain the realistic profiles observed by Bitsanis *et al* [33, 34, 35] and Manias *et al* [36] one needs to reformulate the problem using the inhomogeneous kernel. $\eta_k(\mathbf{r},\mathbf{r}-\mathbf{r}')$

## 5. Conclusions

A review has been presented of some recent progress made in nonequilibrium MD for three types of systems: dendrimers under homogeneous shear flow, indefinite spatio-temporal simulations of elongational flow, and flow in nano-confined fluids. We find that the viscoelastic properties of dendrimers are significantly different than those for linear polymers of equivalent molecular weight and attribute these differences to the more constrained and compact structure of dendrimer molecules. Their usefulness as viscosity modifiers for traditional polymers and alkanes is promising for tribology applications. Work is currently under way to study the viscoelastic properties of systems of dendrimers in solution and blends of linear polymers and dendrimers. In the case of elongational flow we find that use of the famous Arnold cat map as periodic boundary conditions allows us to simulate elongational flow for indefinite times. The cat map formalism is mathematically simpler and more intuitive than the original algebraic derivation of Kraynik and Reinelt [14] and also gives one greater insight into the stability of such flows. We are now studying how microscopic chaos affects the macroscopic flow characteristics for simple atoms and polymeric fluids under elongational flow. Finally, we showed how a generalisation of the Navier–Stokes formalism, made by incorporating a non-local constitutive relation into the momentum continuity equation, enables us to compute an effective position-dependent viscosity that is defined for systems arbitrarily far from equilibrium. Suitable generalisations of the mass and energy conservation equations could assist in the understanding of mass and energy transport in nano-confined fluids. The most useful application of such microscopic techniques may well lie in their incorporation into mesoscopic models of fluid transport, currently a topic of substantial interest.

## References


[1] J.T. Bosko, B.D. Todd, R.J. Sadus. Internal structure of dendrimers in the melt under shear: a molecular dynamics study. *J. Chem. Phys.*, **121**, 1091 (2004).

[2] J.T. Bosko, B.D. Todd, R.J. Sadus. Viscoelastic properties of dendrimers in the melt from nonequilibrium molecular dynamics. *J. Chem. Phys.*, **121**, 12050 (2004).

[3] H.R. Warner Jr. Kinetic theory and rheology of dilute suspensions of finitely extensible dumbbells. *Ind. Eng. Chem. Fundam.*, **11**, 379 (1972).

[4] G.S. Grest, K. Kremer. Molecular dynamics simulation for polymers in the presence of a heat bath. *Phys. Rev. A*, **33**, 3628 (1986).

[5] J.D. Weeks, D. Chandler, H.C. Anderson. Role of repulsive forces in determining the equilibrium structure of simple liquids. *J. Chem. Phys.*, **54**, 5237 (1971).

[6] D.J. Evans, G.P. Morriss. *Statistical Mechanics of Nonequilibrium Liquids*, Academic Press, London (1990).

[7] A.W. Lees, S.F. Edwards. The computer study of transport processes under extreme conditions. *J. Phys. C*, **5**, 1921 (1972).

[8] R. Edberg, D.J. Evans, G.P. Morriss. Constrained molecular dynamics: simulations of liquid alkanes with a new algorithm. *J. Chem. Phys.*, **84**, 6933 (1986).

[9] K.P. Travis, P.J. Daivis, D.J. Evans. Computer simulation algorithms for molecules undergoing planar Couette flow: a nonequilibrium molecular dynamics study. *J. Chem. Phys.*, **103**, 1109 (1995).

[10] R. Scherrenberg, B. Coussens, P. van Vliet, G. Edouard, J. Brackman, E. de Brabander. The molecular characteristics of poly(propyleneimine) dendrimers as studied with small-angle neutron scattering, viscosimetry, and molecular dynamics. *Macromolecules*, **31**, 456 (1998).

[11] M. Doi, S.F. Edwards. *The Theory of Polymer Dynamics*, Clarendon Press, Oxford (1986).

[12] P. de Gennes. Concept of reptation for a polymeric chain. *J. Chem. Phys.*, **55**, 572 (1971).

[13] M. Kröger, S. Hess. Rheological evidence for a dynamical crossover in polymer melts via nonequilibrium molecular dynamics. *Phys. Rev. Lett.*, **85**, 1128 (2000).

[14] A.M. Kraynik, D.A. Reinelt. Extensional motions of spatially periodic lattices. *Int. J. Multiphase Flow*, **18**, 1045 (1992).

[15] B.D. Todd, P.J. Daivis. Nonequilibrium molecular dynamics simulations of planar elongational flow with spatially and temporally periodic boundary conditions. *Phys. Rev. Lett.*, **81**, 1118 (1998).

[16] B.D. Todd, P.J. Daivis. A new algorithm for unrestricted duration molecular dynamics simulations of planar elongational flow. *Comput. Phys. Commun.*, **117**, 191 (1999).

[17] A. Baranyai, P.T. Cummings. Steady-state simulation of planar elongational flow by nonequilibrium molecular dynamics. *J. Chem. Phys.*, **110**, 42 (1999).

[18] P.J. Daivis, M.L. Matin, B.D. Todd. Nonlinear shear and elongational rheology of model polymer melts by non-equilibrium molecular dynamics. *J. Non-Newtonian Fluid Mech.*, **111**, 1 (2003).

[19] T.A. Hunt, B.D. Todd. On the Arnold cat map and periodic boundary conditions for planar elongational flow. *Mol. Phys.*, **101**, 3445 (2003).

[20] V.I. Arnold, A. Avez. *Ergodic problems of classical mechanics*, Benjamin, New York (1968).

[21] J. Petravic, D.J. Evans. Approach to the nonequilibrium time-periodic state in a steady shear flow model. *Mol. Phys.*, **95**, 219 (1998).

[22] B.D. Todd, P.J. Daivis. Elongational viscosities from nonequilibrium molecular dynamics simulations of oscillatory elongational flow. *J. Chem. Phys.*, **107**, 1617 (1997).

[23] M.W. Evans, D.M. Heyes. Combined shear and elongational flow by non-equilibrium molecular dynamics. *Mol. Phys.*, **69**, 241 (1990).

[24] M.E. Tuckerman, C.J. Mundy, S. Balasubramanian, M.L. Klein. Modified nonequilibrium molecular dynamics for fluid flows with energy conservation. *J. Chem. Phys.*, **106**, 5615 (1997).

[25] D.J. Evans, D.J. Searles, W.G. Hoover, C.G. Hoover, B.L. Holian, H.A. Posch, G.P. Morriss. Comment on: Modified nonequilibrium molecular dynamics for fluid flows with energy conservation [J. Chem. Phys., 106 (1997) 5615]. *J. Chem. Phys.*, **108**, 4351 (1998).

[26] A. Katok, B. Hasselblatt. *Introduction to the modern theory of dynamical systems*, Cambridge University Press, Cambridge (1995).

[27] H.M. Laun, M. Münstedt. Elongational behaviour of a low density polyethylene melt. I. Strain rate and stress dependence of viscosity and recoverable strain in the steady state. Comparison with shear data. Influence of interfacial tension. *Rheol. Acta*, **17**, 415 (1978).

[28] B.D. Todd, P.J. Daivis. The stability of nonequilibrium molecular dynamics simulations of elongational flows. *J. Chem. Phys.*, **112**, 40 (2000).

[29] B.D. Todd, D.J. Evans, P.J. Daivis. Pressure tensor for inhomogeneous fluids. *Phys. Rev. E*, **52**, 1627 (1995).

[30] J. Zhang, B.D. Todd, K.P. Travis. Viscosity of confined inhomogeneous nonequilibrium fluids. *J. Chem. Phys*, **121**, 10778 (2004). Erratum, in press (2005).

[31] K.P. Travis, B.D. Todd, D.J. Evans. Departure from Navier–Stokes hydrodynamics in confined liquids. *Phys. Rev. E*, **55**, 4288 (1997).

[32] K.P. Travis, K.E. Gubbins. Poiseuille flow of Lennard–Jones fluids in narrow slit pores. *J. Chem. Phys.*, **112**, 1984 (2000).
[33] I. Bitsanis, J.J. Magda, M. Tirell, H.T. Davis. Molecular dynamics of flow in micropores. *J. Chem. Phys.*, **87**, 1733 (1987).
[34] I. Bitsanis, T.K. Vanderlick, M. Tirell, H.T. Davis. A tractable molecular theory of flow in strongly inhomogeneous fluids. *J. Chem. Phys.*, **89**, 3152 (1988).
[35] I. Bitsanis, S.A. Somers, H.T. Davis, M. Tirell. Microscopic dynamics of flow in molecularly narrow pores. *J. Chem.*, **93**, 3427 (1990).
[36] E. Manias, I. Bitsanis, G. Hadziioannou, G. ten Brinke. On the nature of shear thinning in nanoscopically confined films. *Europhys. Lett.*, **33**, 371 (1996).
[37] J.C. Sprott. *Chaos and Time Series Analysis*, Oxford University Press, Oxford (2003).